# Combustion Noise Dependency on Thermal Load and Global Equivalence Ratio in a Swirl-Stabilized Combustor

F. Grimm* , F. Setzwein† , S. Werner‡ , M. Stöhr§ , B. Noll¶ , M. Aigner‖
*Institute of Combustion Technology*
*German Aerospace Center (DLR)*
*Pfaffenwaldring 38-40, 70569 Stuttgart, Germany*

R. Ewert** ,J. Dierke††
*Institute of Aerodynamics and Flow Technology, Technical Acoustics*
*German Aerospace Center (DLR)*
*Lilienthalplatz 7, 38108 Braunschweig, Germany*

**A laboratory scale, swirl stabilized burner is investigated in view of the impact of global equivalence ratio and thermal power variation on broadband combustion noise emission. The PRECCINSTA burner (Prediction and Control of Combustion Instabilities in Industrial Gas Turbines) is operated at atmospheric conditions. The presented combustion noise studies are based on a perfectly premixed configuration, where methane is burnt with air.**
**From experiments, newly measured sound pressure spectra in the combustion system with well-defined acoustic boundary conditions are presented for several thermal loads and global equivalent ratios.**
**For the combustion noise simulations, the hybrid CFD/CCA approach 3D FRPM-CN (Fast Random Particle Method for Combustion Noise Prediction) is used. Numerical simulation results of CFD and combustion acoustics are compared with experimental data in terms of flow field and combustion. 3D FRPM-CN is then assessed for its prediction capability of effects of combustion parameter variation on broadband noise emission. Numerical results are interpreted with a method for spectral mode decomposition. High frequency acoustic modes in the combustion chamber are identified and characterized.**
**Sound pressure spectra from numerical simulations are evaluated with experimental data in view of reproduction of absolute direct combustion noise levels and shape of spectra. With the study presented in this work, not only a combustion noise prediction tools is further validated, but also a large experimental data base for combustion noise and thermo-acoustics validation in swirl-stabilized, confined configurations is introduced.**

## I. Introduction

The investigation of noise emission in aviation has become a prevailing research topic. This is motivated besides other things by institutional requirements regarding noise emissions of airplanes in civil aviation [1–3].
There are a large number of relevant noise sources in aircrafts, whereas the engine contributes a significant fraction to overall noise levels [4]. Numerous research efforts addressing the understanding of noise generation mechanisms and consequently the development of efficient noise reduction strategies for components like fan, compressor and exhaust jet led to an increased significance of combustion noise [5] and therefore a greater need to gain understanding of noise generation mechanisms and to find measures for its reduction.
From today's standpoint, there is still deficiency in the theoretical and physical understanding of combustion noise [6]. Therefore, many studies address the issue with empirical approaches. In principle, combustion acoustics can be

*Research Engineer, DLR, Institute of Combustion Technology, Stuttgart, Germany
†Research Engineer, DLR, Institute of Combustion Technology, Stuttgart, Germany
‡Research Engineer, DLR, Institute of Combustion Technology, Stuttgart, Germany
§Research Engineer, DLR, Institute of Combustion Technology, Stuttgart, Germany
¶Research Engineer, DLR, Institute of Combustion Technology, Stuttgart, Germany
‖Professor, DLR, Director of the Institute of Combustion Technology, Stuttgart, Germany
**Research Engineer, DLR, Institute of Aerodynamics and Flow Technology, Technical Acoustics, Braunschweig, Germany
††Research Engineer, DLR, Institute of Aerodynamics and Flow Technology, Technical Acoustics, Braunschweig, Germany

modeled from fully or partially scale resolving simulations, which also allow for the caption of thermoacoustic phenomena. However, direct methods are computationally extremely expensive. Therefore, hybrid CFD/CAA approaches are an attractive alternative, since they provide a large potential for saving computational resources. Furthermore, analyzing a problem with hybrid methods gives the possibility to apply specifically optimized methods to subproblems [7] and allow for manifold analyses, although acoustic feedback phenomena cannot be directly resolved. Here, at first, steady state, reacting CFD simulations of different burner operation conditions are conducted with the DLR inhouse code THETA (Turbulent Heat Release Extension of the TAU Code). A stochastic combustion noise sound source reconstruction approach subsequently uses averaged flow field and turbulence statistics from CFD simulations. Sound propagation is simulated with the DLR inhouse code PIANO (Perturbation Investigation of Aerodynamic Noise) via linearized Euler equations with local right hand side forcing based on reconstructed combustion noise sources.
The approach of combustion noise modeling utilized in this work was derived by Mühlbauer et al. [8], using the sound source reconstruction algorithm from Ewert [9–12]. In recent works it was further developed by Grimm et al. [13, 14] for the applicability to complex test cases. The employed physical source term model was derived from first principles, using a fundamental pressure-density relation, leading to the linearized Euler energy equation with a right hand side forcing [15], where the complete right hand side source expression of the pressure-density relation was taken from Candel et al. [16]. Their comprehensive source term was condensed to a temperature-variance based, monopole source term expression.
In this work, the impact of a variation of combustion parameters on sound pressure spectra in a laboratory scale model combustor is studied in order to provide a more detailed data base serving for the understanding of how differently combustion parameters influence noise production in a swirl stabilized burner. In this context, a hybrid CFD/CCA stochastic method for combustion noise prediction is tested for its applicability and prediction capability towards a variation of those combustion parameters and a novel data set of acoustics measurements of this burner is presented. Therefore, combustion noise dependency on thermal load and global equivalence ratio is assessed with experimental and numerical methods for a complex, swirl stabilized and encased burner configuration.
At first, models and analysis tools used for the theoretical and numerical studies are explained. This is followed by an introduction of the investigated combustor, the PRECCINSTA burner. The experimental measurement techniques, consisting of acoustic pressure measurements, Raman measurements for the temperature field and species distribution, and PIV (Particle Image Velocimetry) for information on the combustor flow field are not explicitly introduced. A deeper focus lies on the theoretical analysis of combustion noise in the burner system. Details on experimental setups can be found in the literature [17–19]. The CFD setup and the treated test cases are explained in detail, before those fluid dynamics numerical tools are validated for a reference operation case at a thermal load of $P_{th}$ = 25kW and a global equivalence ratio of $\Phi = 0.9$. Validation is carried out by means of velocity, and temperature distributions in the combustion chamber [17–19]. Consistency of the results of combustion parameter variation is demonstrated by means of correlating thermal load and equivalence ratio with integral heat release and integral effective combustion noise source variance.
After CFD results are depicted for all treated operational variations, the CCA (Computational Combustion Acoustics) setup is explained. An effective combustion noise source term realization is identified, which can be extracted solely from the known CFD statistical quantities. It is used to establish correlations between integral turbulence statistics and the resulting combustion noise source entry into the burner system. Finally, combustion acoustics results are discussed with a method for spectral decomposition and it is shown that input turbulence statistics to 3D FRPM-CN are nicely reproduced in this complex application case. The comparison of numerically and experimentally obtained sound pressure spectra reveals that 3D FRPM-CN reproduces absolute combustion noise levels and reproduces the spectral distribution of combustion noise fairly accurately.

## II. Computational Fluid Dynamics Framework

Reacting CFD simulations are carried out with the finite volume based DLR inhouse code THETA (*Turbulent Heat Release Extension of the TAU Code*) [20]. A detailed description of the main THETA code features can be found in the literature [21–23]. The code is designed for the simulation of steady and unsteady turbulent reacting flows with an incompressible solver on unstructured meshes using a dual-grid approach. A description of the governing equations and employed turbulence and combustion models for this specific laboratory scale burner case can be found in Grimm et al. [24]. A comprehensive numerical study using a compressible extension of the THETA code was performed by Lourier et al. [25], where thermoacoustic phenomena occurring in this test case were investigated.

## III. Modeling of Turbulent Combustion Noise

A combustion noise monopole source term based model is applied to a laboratory scale, single sector combustor operating in perfectly premixed mode. The source term model was introduced originally by Mühlbauer et al. [26] and further developed by Grimm et al. [27]. The following two sections, explaining the source term formulation, acoustic model and sound source reconstruction approach are taken from Grimm et al. [24] and are given here for completeness.

**Source Term Formulation and Acoustic Model**

The basis for the source term formulation derivation is a pressure-density relation

$$\frac{1}{c^2}\frac{Dp}{Dt} = \frac{D\rho}{Dt} + \rho\Phi \tag{1}$$

with a right hand side expression $\Phi$ from Candel et al. [16], reading

$$\begin{aligned}\Phi =& \frac{\dot{Q}}{\rho c_p T} + M\frac{D}{Dt}\left(\frac{1}{M}\right) + \\ & \frac{1}{\rho c_p T}\left[\nabla\cdot\lambda\nabla T + \boldsymbol{\tau_\tau} : \nabla\mathbf{u} - \sum_{\alpha=1}^{N_s}\rho Y_\alpha c_{p,\alpha}\mathbf{V}_\alpha^D\cdot\nabla T\right],\end{aligned} \tag{2}$$

with $\lambda$, the heat conductivity and $\mathbf{V}_\alpha^D$, the diffusion velocity of species $\alpha$. $\dot{Q}$ is the volumetric heat release rate and $M$ denotes the molecular weight. Eq. (2) is reformulated by making use of the energy equation, leading to a formulation with the heat release rate expressed in terms of temperature change

$$\Phi = \frac{1}{T}\frac{DT}{Dt} - \frac{1}{\rho c_p T}\frac{Dp}{Dt} + M\frac{D}{Dt}\left(\frac{1}{M}\right). \tag{3}$$

According to Mühlbauer et al. [26], this formulation is a complete representation of the source term as given by Eq. (2). Since usually applications with low Mach number flows are treated, the first term in Eq. (3) is assumed to be dominant over the second, representing the effects of turbulent velocity fluctuations and the second term is therefore neglected. The third term in Eq. (3) comes into picture only if the average molecular weight of combustion products significantly differs from the educts and is therefore also not considered here for the application of methane-air combustion systems.

Based on the first term of Eq. (3), a right hand side processing rule for the source term expression is obtained by transferring a pressure equation formulation

$$\frac{Dp}{Dt} + \gamma p\nabla\cdot\mathbf{u} = \gamma p\Phi, \tag{4}$$

with the isentropic exponent $\gamma = c_p/c_v$, to the pressure equation form of the linearized Euler equations [15]. This procedure gives $q_p = (\gamma p\Phi)' = \rho c^2\Phi - \overline{\rho c^2\Phi}$, which is then applied to the simplification of Eq. (3). The resulting, temperature variance based source term expression, which is subject to FRPM-CN modeling, reads

$$q_p = \frac{\gamma\overline{p}}{\tilde{T}}\frac{\tilde{D}T''}{Dt}. \tag{5}$$

For the application of the full scale laboratory combustor simulation, it is coupled with a modified form of the linearized Euler equations

$$\frac{\partial\rho'}{\partial t} + \widetilde{\boldsymbol{u}}\cdot\nabla\rho' + \overline{\rho}\nabla\cdot\boldsymbol{u}' = 0 \tag{6}$$

$$\frac{\partial\boldsymbol{u}'}{\partial t} + \left(\widetilde{\boldsymbol{u}}\cdot\nabla\right)\boldsymbol{u}' + \frac{\nabla p'}{\overline{\rho}} = \mathbf{0} \tag{7}$$

$$\frac{\partial p'}{\partial t} + \widetilde{\boldsymbol{u}}\cdot\nabla p' + \gamma\overline{p}\nabla\cdot\boldsymbol{u}' = q_p, \tag{8}$$

with the source term (Eq. (5)) on the right hand side of the pressure equation (Eq. (8)). Eqs. (6) to (8) represent the linearized Euler equations, while meanflow gradient terms are not taken into consideration. As stated by Ewert et al. [28], those components are assigned to causing instabilities in the LEEs. As observed for the herein treated application case, this is mainly dependent on the local characteristics of the background flow field.
Since the employed combustion noise source term formulation is temperature variance based, an additional transport equation for the temperature variance is solved on top of the numerical CFD RANS solution. It reads

$$\overline{\rho}\nabla\cdot(\widetilde{T''^2}\boldsymbol{u}) - \nabla\cdot\left[\left(\frac{\mu}{Pr}+\frac{\mu_t}{Pr_t}\right)\nabla\widetilde{T''^2}\right] = 2\frac{\mu_t}{Pr_t}(\nabla\widetilde{T})^2 - \overline{\rho}C_T\frac{\widetilde{T''^2}}{\tau_T}, \tag{9}$$

with the model constant $C_T = 2.$ $\mu$ and $Pr$ are the viscosity and the Prandtl number. The indexes $t$ and $T$ mean turbulent and turbulent temperature associated. The $\sim$ denotes Favré averaging.

**Stochastic Reconstruction of Sound Sources**

The source term in Eq. (5) is subject to stochastic sound source reconstruction. Therefore, the Fast Random Particle Method for Combustion Noise (FRPM-CN), introduced by Grimm et al. [27, 29], is employed. Sound sources are built for each time-step according to local turbulence statistics from convective white noise. This noise field is realized in a discrete form by mapping random values carried by floating particles onto a source field grid. The spatial extensions of the source field are chosen according to the characteristics of the solution of Eq. (9). The spatial filtering algorithm of sources can be generally described by

$$Q(\boldsymbol{x},t) = \int_{V_s}\hat{A}(\boldsymbol{x})\mathcal{G}(|\boldsymbol{x}-\boldsymbol{x}'|,l_T(\boldsymbol{x}))\mathcal{U}(\boldsymbol{x}',t)d^3\boldsymbol{x}'. \tag{10}$$

The discretization with FRPM instead of a preceding, streamline based approach RPM [15], features an initialization with particles in the whole source region and therefore provides the resolution of recirculation zones. Furthermore, the FRPM grid is orthogonal in contrary to the streamline-based RPM discretization and therefore highly efficient Purser filter [30, 31] are employed for the source filtering, represented by $\mathcal{G}$, which is convoluted with a white noise field $\mathcal{U}$. Integration of source components is performed over the source volume $V_s$ and the local amplitude scaling is realized according to $\hat{A} = \sqrt{\hat{R}(\boldsymbol{x})/l_T^3(\boldsymbol{x})}$, in order to achieve the appropriate local source variance. The spatial white noise field $\mathcal{U}$ is processed with a first order Langevin approach in time for the realization of turbulence induced decay,

$$\frac{D_0}{Dt}\mathcal{U} = -\frac{1}{\tau_T}\mathcal{U} + \sqrt{\frac{2}{\tau_T}}\xi(\boldsymbol{x},t). \tag{11}$$

Equation (11) is a stochastic differential equation, realizing a long-term drift behaviour with the first component on the right hand side, while the second - so called diffusion term - introduces a Gaussian distributed white noise forcing, for which the random values have to be chosen appropriately [11]. $D_0/Dt = \partial/\partial t + \boldsymbol{u}_0^c\cdot\nabla$ and $\boldsymbol{u}_0^c$ is the mean CFD RANS velocity field. For $\xi(\boldsymbol{x},t)$, the properties

$$\langle\xi(\boldsymbol{x},t)\rangle = 0, \tag{12}$$

$$\langle\xi(\boldsymbol{x},t)\xi(\boldsymbol{x}+\boldsymbol{r},t+\tau)\rangle = \delta(\boldsymbol{r}-\boldsymbol{u}_0^c\tau)\delta(\tau) \tag{13}$$

hold. The brackets $\langle\rangle$ denote ensemble-averaging. For small separation distance $\boldsymbol{r}$ and time $\tau$, the noise field $\mathcal{U}$ correlation can be expressed by taking into account the solution of Eq. (11) and the source statistics from Eq. (13), as

$$\langle\mathcal{U}(\boldsymbol{x},t)\mathcal{U}(\boldsymbol{x}+\boldsymbol{r},t+\tau)\rangle = \delta(\boldsymbol{r}-\boldsymbol{u}_0^c\tau)\exp\left(-|\tau|/\tau_T\right), \tag{14}$$

or in words, the Langevin process induces an exponential decorrelation, representing turbulence related decay. The overall FRPM-inherent correlation function, resulting from the Langevin-induced decorrelation and the use of a Gaussian-shaped filter for the sound reconstruction procedure resulting from Eq. (10), reads

$$\mathcal{R}(\boldsymbol{x},\boldsymbol{r},\tau) = \hat{R}(\boldsymbol{x})\exp\left(-\frac{|\tau|}{\tau_T}-\frac{\pi}{4l_T^2(\boldsymbol{x})}|\boldsymbol{r}-\boldsymbol{u}_0^c\tau|^2\right). \tag{15}$$

Equation (15) is used as the correlation function of combustion noise sources for the presented numerical simulations with $\hat{R}(\boldsymbol{x}) = \overline{T''^2(\boldsymbol{x})}/\tau_T(\boldsymbol{x})^2$. $\boldsymbol{r}$ and $\tau$ in Eq. (15) are the separation distance and time, respectively, while $\tau_T$ and $l_T$ are the local turbulent time- and length-scale, herein taken from the preceding reacting CFD RANS solution.

## IV. Spectral Fourier Filtering

As a tool for mode decomposition and system identification in dynamic systems with frequency dependent phenomena, a Selective Fast Fourier Filtering Approach (SFFFA) as introduced in [32] is applied. It is used to identify dynamics in the acoustic pressure fluctuations in the investigated combustion chamber and to depict turbulent time-scale dependency of acoustic noise source fluctuations in the results sections.

The method is based on frequency-filtered analysis of transient, time-coherent data from spatially distributed monitoring points in either Fourier-space or time-domain. At first, $N_P$ monitoring points are defined in a domain, where fluctuating acoustics quantities are monitored as a series of discrete time points. Those quantities are represented by the variable $\Phi_k$ at positions $\boldsymbol{x}_i$. $k$ defines a discrete point in time. Signals are recorded over a time-period $t_{\mathrm{Sig}}$, resulting in $N = t_{\mathrm{Sig}}/\Delta t$ recorded equidistant time-points with a time-step $\Delta t$.

Consecutively, the respective complex, Fourier transform of the signal $\hat{\Phi}_m$ with $m = 0, ..., N-1$ is evaluated, where $m$ is assigned to a discrete frequency $f_m$. The numerical algorithm of the Fourier transform is commonly known as discrete Fourier transform (DFT), and is evaluated from [33]

$$\hat{\Phi}_m = \frac{1}{N} \sum_{k=0}^{N-1} \Phi_k \exp(-2\pi i \frac{mk}{N}), \quad m = 0, ..., N-1. \tag{16}$$

The computational time of a DFT according to Eq. (16) increases with the number of samples to $O(N^2)$. For efficiency reasons, the Fast Fourier Transform (FFT) algorithm of Cooley and Tukey [34] is used instead, resulting in a computational turnaround of $O(N \log N)$. With the FFT, the signal energy is effectively distributed to a frequency spectrum. The maximum resolved frequency is defined by the Nyquist criterion,

$$f_{\max} = f_s/2 = 1/(2\Delta t), \tag{17}$$

with the sampling rate $f_s$. In the following, the resolvable part of the spectrum $f_m$ with $m = 0, ..., (N-1)/2$ is treated, where $f_{(N-1)/2} = f_{\max}$ equals the Nyquist frequency. For conservation of signal energy, the entries $m = 1, ..., (N-1)/2 - 1$ of the quantities $\hat{\Phi}_m$ have to be multiplied with a factor 2 [33, 35].

Subsequently, a high- and low-pass filter is applied to $\hat{\Phi}_m$, filtering out values assigned to frequencies outside of $[f_{\min}, f_{\max}]$,

$$\hat{\Phi}_{\mathrm{Filt},m} = \begin{cases} \hat{\Phi}_m & \text{for} \quad f_{\min} \leq f_m \leq f_{\max} \\ 0 & \text{else.} \end{cases} \tag{18}$$

For the complex, filtered signal $\hat{\Phi}_{\mathrm{Filt},m} = a_m + i \cdot b_m = A_m \exp(i\varphi_m)$, the respective amplitudes $A_m = \sqrt{a_m^2 + b_m^2}$ and angles $\varphi_m = \tan^{-1}(b_m/a_m)$ are computed. Further on, the filtered signal is back-transformed to time-domain for a discrete time-point $t_k$, using the relation [35]

$$\Phi_{\mathrm{Filt},k} = \mathrm{Im}\left( \sum_{m=0}^{\frac{N-1}{2}} A_m e^{i(2\pi f_m t_k + \varphi_m)} \right). \tag{19}$$

The complete time period of the filtered signal for a full cycle results to $t_{\mathrm{Filt}} = 1/f_{\min}$. Therefore, a discrete time-point $t_k$ within a period of the filtered signal is defined as

$$t_k = t_{\mathrm{Filt}} \cdot \frac{\alpha}{2\pi}, \tag{20}$$

with $\alpha = [0, 2\pi]$ meaning an arbitrary phase angle of the oscillation. The resulting signal value for a phase angle $\alpha$ of the filtered oscillation amounts to

$$\Phi_{\mathrm{Filt},\alpha} = \mathrm{Im}\left( \sum_{m=0}^{\frac{N-1}{2}} A_m e^{i\left(\alpha \frac{f_m}{f_{\min}} + \varphi_m\right)} \right). \tag{21}$$

For the depiction of a change in time of the filtered field, Eq. (21) is used to compute $N_{PA}$ different phase angles and their quadratic average is constructed by

$$\Phi_{\text{Filt, RMS}} = \sqrt{\frac{1}{N_{PA}} \cdot \sum_{i=0}^{N_{PA}} \Phi_{\text{Filt},i}^2}. \tag{22}$$

An example for selective Fourier filtering is shown in Fig. 1. The original signal in red (left) is transformed to Fourier space (right). Subsequently, a low frequency band of interest is maintained in the reconstructed signal, leading to a low-pass filter and a highly smoothed reconstructed signal.

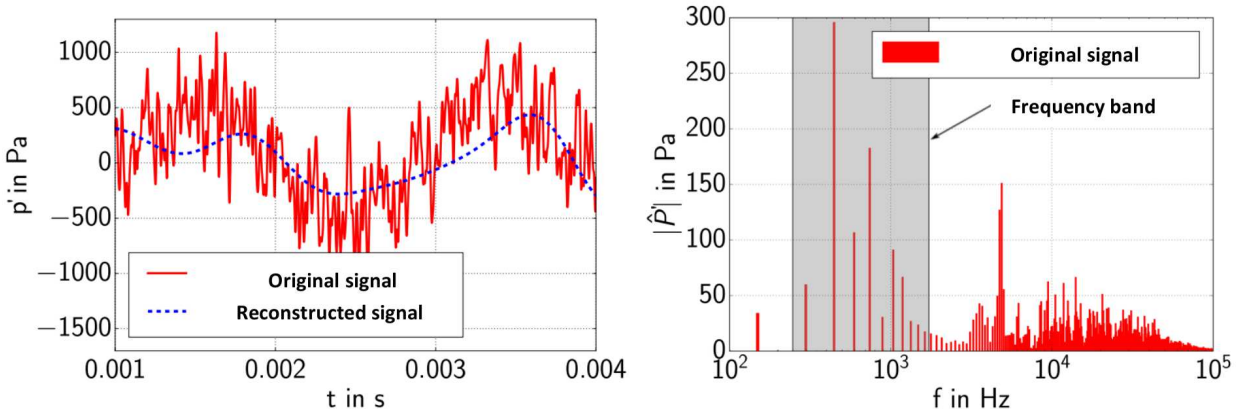


**Fig. 1 Generic example for selective Fourier filtering. Time domain original and resulting signal (left) and frequency domain signal with filtered frequency band (right).**

## V. Laboratory Scale Combustor Application Case

The numerically investigated PRECCINSTA (Prediction and Control of Combustion Instabilities in Industrial Gas Turbines) burner is schematically shown in Fig. 2a. The numerical simulations are validated based on an experimental reference study with technical and perfect premixing by Dem et al. [17]. The investigations in this framework are focused on perfectly premixed combustion. The burner works as follows:
An air plenum is mounted upstream. The air-fuel mixture is led into the plenum and consecutively through a swirler into the combustion chamber. The radial swirler consists of 12 swirler vanes. The fuel plenum as indicated in Fig. 2a serves for injection of fuel to air in a technically premixed operation mode [17]. For perfectly premixed combustion it is present as part of the burner geometry without further purpose. The tip of the conical center body prior to the combustion chamber denotes the reference point of the global coordinate system, as indicated in Fig. 2b. Subsequently, the air-fuel mixture expands into the combustion chamber, which has the dimensions $114\text{mm} \times 85\text{mm} \times 85\text{mm}$. There, a swirl-stabilized flame is located. The burnt gas exits the combustion chamber through a converging section followed by an exhaust duct of $d = 40mm$. A detailed description of the experimental setup can be found in the literature [17].

Comparison of CFD results is carried out for the flow field with averaged results from stereoscopic particle image velocimetry (PIV) [17, 18] of all three velocity components at horizontal profile lines in the combustion chamber at $h = 6\text{mm}, 10\text{mm}, 20\text{mm}, 40\text{mm}$. Single-shot laser Raman scattering measurements [19] are available for temperature profile lines and the mean species concentrations ($O_2, CH_4, CO_2, H_2O$) at the same positions for validation of CFD combustion and reaction mechanism.
Acoustic pressure measurements are available for a wide range of operation conditions. For the microphone measurements, quartz-glass windows for optical access are replaced with fixed metal walls, in order to exclude possible wall damping effects and to ensure consistency with simulation boundary conditions. Fluctuating acoustic pressure is sampled at a combustion chamber reference microphone position at $z = 42.5\text{mm}, y = r = 42.5\text{mm}, x = h = 15\text{mm}$ and in the upstream air-fuel plenum at $z = 34.2\text{mm}, y = r = 19.75\text{mm}, x = h = -76\text{mm}$.

The plenum microphone is directly mounted to the arrangement, while the combustion chamber microphone is set off to the burner by a small tube, due to high temperatures in the reaction zone. Measurement of acoustic pressure is

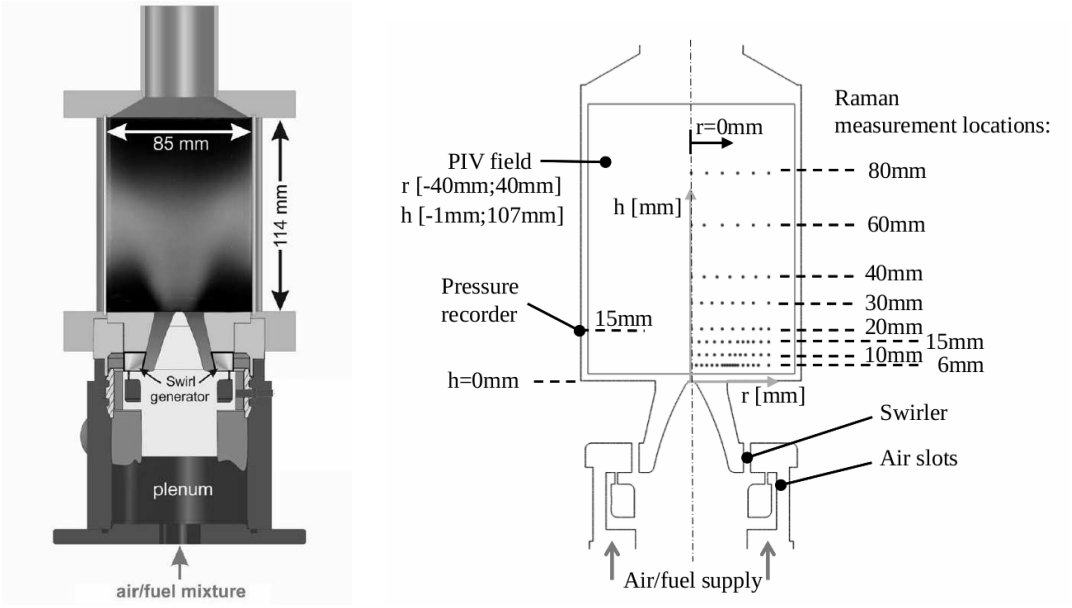


(a) Schematic drawing of the burner [17].

(b) Spatial conventions and measurement locations for Raman and PIV.

**Fig. 2 Schematic drawing of the investigated PRECCINSTA burner and measurement locations.**

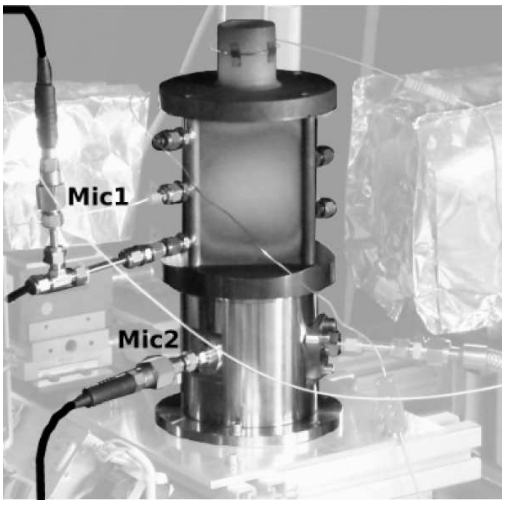


**Fig. 3 Experimental setup for acoustic pressure measurements.**

then carried out in tube-normal direction and cooling flow is present in this small duct. Therefore, recorded acoustic pressure is corrected with a specific calibration function. The sampling rate of signals is $f_s = 50$kHz.

## VI. CFD Setup

The unstructured grid for the reacting CFD RANS simulations [36] is shown in Fig. 4. The regions of the reaction zone as well as the swirler vanes and the connecting ribs between air plenum and combustor are refined compared to the air plenum and downstream zones in the combustion chamber and the exhaust tube. The inner computational domain is entirely discretized with tetrahedra. Near wall regions in the swirler and combustion chamber are covered with three prism layers and they are interconnected to the inner domains via pyramid elements. The tetrahedral grid consists of 16.6M elements with 2.9M points. Furthermore, it consists of 0.47M prism elements and 5K pyramids.

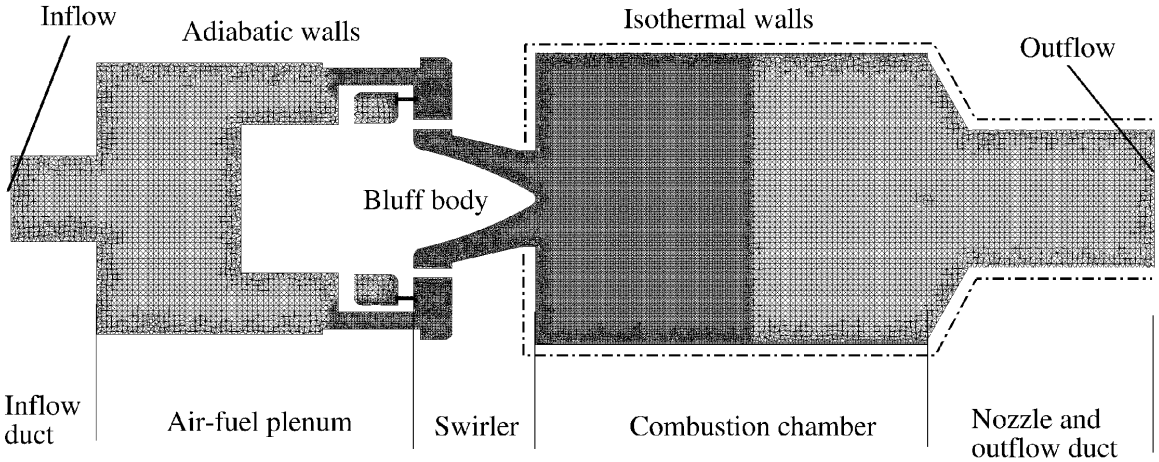


**Fig. 4 CFD computational grid with applied boundary conditions and labeled burner sections [37].**

The simulations are carried out with the finite volume based DLR research code THETA [21, 38]. The reacting CFD RANS calculations are based on an incompressible formulation of the Navier Stokes equations, treated with a SIMPLE (Semi-Implicit Method for Pressure Linked Equations) solution procedure. For the spatial discretization of the steady state RANS simulations, a second order accurate scheme (QUDS) is used. The physical time-step of the URANS simulations is $\Delta t = 5 \cdot 10^{-5}$s. For turbulence modeling, the $k\omega$-SST approach [39] is employed.

Mass flow is specified at the upstream air-fuel inlet with a turbulence degree of $Tu = 0.01$ and an initial turbulent length-scale $l_T = 1 \cdot 10^{-4}$m, respectively, at $T_{in} = 320$K. At the combustion chamber outlet tube, the static pressure is set to ambient reference conditions. Walls are treated as adiabatic except for isothermal combustion chamber walls, as indicated in Fig. 4, impinged with $T_W = 1200$K.

Monitoring positions of the mean flow field and combustion quantities are horizontal profile lines according to the respective PIV measurements at $h = 0.006\text{m}, 0.01\text{m}, 0.02\text{m}, 0.04\text{m}$. As a solution strategy, at first, steady state reacting simulations are carried out. In order to accurately predict chemical reactions, an URANS simulation with a physical time-step is attached. Combustion is treated with a combined EDM/FRC approach for global reaction schemes. In this work, methane is burned with air under atmospheric conditions. This is depicted with a five-step global reaction scheme originally proposed by Nicol et al. [40]. It was optimized with respect to the laminar flame speed and is therefore a modified version of the published scheme. On top of the solution of flow field and combustion, an additional transport equation, Eq. (9), for the determination of a field solution for the temperature variance is solved. Therefrom, the local source term fluctuation amplitudes in the subsequent CCA simulations are determined.

Investigated operation conditions are listed in Table 1. A variation of thermal load and global equivalence ratio is carried out. The reference case of $P_{\text{th}} = 25\text{kW}, \Phi = 0.9$ is explicitly compared to experimental data of flow field and combustion [17]. Applied mass flow rates at the air-fuel inlet are evaluated by using a general reaction equation [41] of the form

**Table 1 Investigated operation conditions and respectively applied mass-flow inlet boundary condition. Reference case: $P_{th} = 25\text{kW}, \Phi = 0.9$. Left: variation of thermal load, right: variation of global equivalence ratio. Mass flow rates in** g/min**.**

| $P_{\text{th}}$[kW] | $\Phi$[−] | $\dot{m}_{\text{Fuel}}$ | $\dot{m}_{\text{Air}}$ | Re [−] | $P_{\text{th}}$[kW] | $\Phi$[−] | $\dot{m}_{\text{Fuel}}$ | $\dot{m}_{\text{Air}}$ | Re [−] |
|---|---|---|---|---|---|---|---|---|---|
| 30 | 0.9 | 36 | 689 | 26450 | 25 | 0.8 | 30 | 646 | 24660 |
| 25 | 0.9 | 30 | 574 | 22042 | 25 | 0.9 | 30 | 574 | 22042 |
| 20 | 0.9 | 24 | 459 | 17633 | 25 | 0.75 | 30 | 689 | 26231 |
| 15 | 0.9 | 18 | 345 | 13225 | 25 | 0.7 | 30 | 738 | 28027 |
| 12.5 | 0.9 | 15 | 287 | 11021 | | | | | |
| 10 | 0.9 | 12 | 230 | 8817 | | | | | |
| 7.5 | 0.9 | 9 | 172 | 6613 | | | | | |
| 5 | 0.9 | 6 | 115 | 4408 | | | | | |

$$\text{CH}_4 + \frac{2}{\Phi}\left(\text{O}_2 + X_{\text{N}_2/\text{O}_2}\text{N}_2\right) \rightarrow \text{CO}_2 + 2\text{H}_2\text{O} + 2\left(\frac{1}{\Phi} - 1\right)\text{O}_2 + \frac{2X_{\text{N}_2/\text{O}_2}}{\Phi}\text{N}_2, \tag{23}$$

with the ratio of molar masses $X_{\text{N}_2/\text{O}_2} = 3.729$. Therefrom, $\dot{m}_{\text{In}} = \dot{m}_{\text{Fuel}} + \dot{m}_{\text{Air}}$ is computed depending on the respective thermal load $P_{th}$ and global equivalence ratio $\Phi$. Species mass fractions at inlet conditions $Y_{\alpha,\text{In}}$ for species $\alpha$ are

$$Y_{\alpha,\text{In}} = \frac{\nu'_\alpha M_\alpha}{\nu'_{\text{CH}_4} M_{\text{CH}_4} + \frac{2}{\Phi}\left(\nu'_{\text{O}_2} M_{\text{O}_2} + X_{\text{N}_2/\text{O}_2}\nu'_{\text{N}_2} M_{\text{N}_2}\right)}, \tag{24}$$

with the stoichiometric coefficients $\nu'_\alpha$ for species $\alpha$, extracted from Eq. (23) and the molar masses $M_\alpha$ for species $\alpha$. Mass flow rates as listed in Table 1 consequently are

$$\dot{m}_{\text{In}} = \dot{m}_{\text{CH}_4} + \dot{m}_{\text{Air}} \quad \text{with} \quad \dot{m}_{\text{Air}} = \dot{m}_{\text{CH}_4}\left(\frac{1}{Y_{\text{CH}_4,\text{In}} - 1}\right) \quad \text{and} \quad \dot{m}_{\text{CH}_4} = \frac{P_{th}}{H_u}. \tag{25}$$

$H_u = 50.013\text{MJ/kg}$ is taken as the calorific value of methane.

As an analysis tool for the expected combustion noise source distribution in the combustion chamber, an additional parameter $\varphi$ is introduced. It is evaluated from the discrete realization of the source term $q_p$ in Eq. (5),

$$\varphi = \frac{\gamma\overline{p}}{\tilde{T}}\sqrt{\frac{\widetilde{T''^2}}{\tau_T^2}}. \tag{26}$$

All quantities from Eq. (26) can be directly extracted from CFD simulations, with $\tau_T = 1/(0.09\omega)$. Therefore, $\varphi$ reveals regions in the combustion chamber, where contributions to combustion noise based on the temperature variance based formulation of Eq. (5) are present. An exemplary evaluation of Eq. (26) for the reference case is shown in Fig. 5. A visual correlation of the data in Table 1 is given in Fig. 6. For the investigated operation points, thermal loads increase with air and fuel mass flow rates and therefore higher inflow velocities. Thermal power is furthermore a function of equivalence ratio. For low investigated thermal loads, a variation in equivalence ratio has a much less pronounced effect than for higher thermal loads. Reynolds number variations and their impact on thermal load and equivalence ratio correspond to velocity inlet variations, as expected.

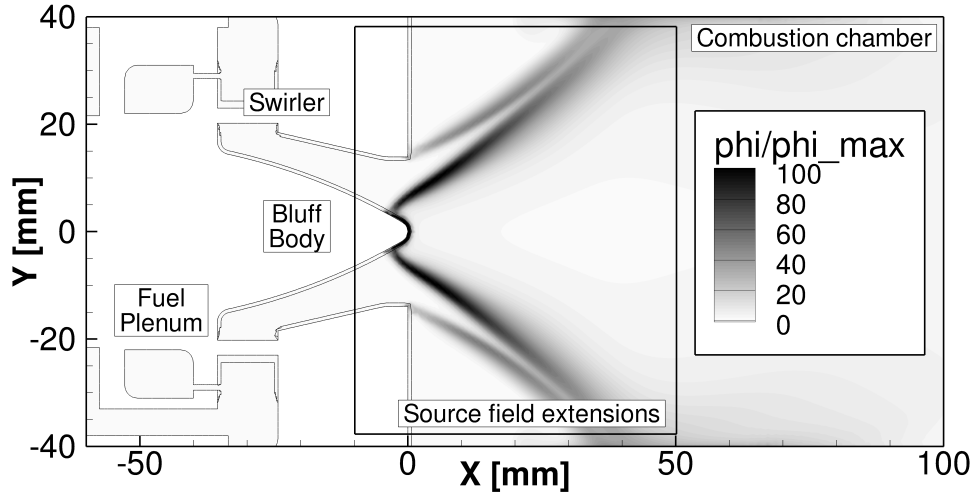


**Fig. 5 Field plot of effectively realized combustion noise sound source standard deviation. Indicator for regions in the combustion chamber contributing to combustion noise. Evaluated from a discrete realization $\varphi = (\gamma\overline{p})/\tilde{T}(\widetilde{T''^2}/\tau_T^2)^{0.5}$ of Eq. (5). Burner rotated clockwise by $90°$ [37].**

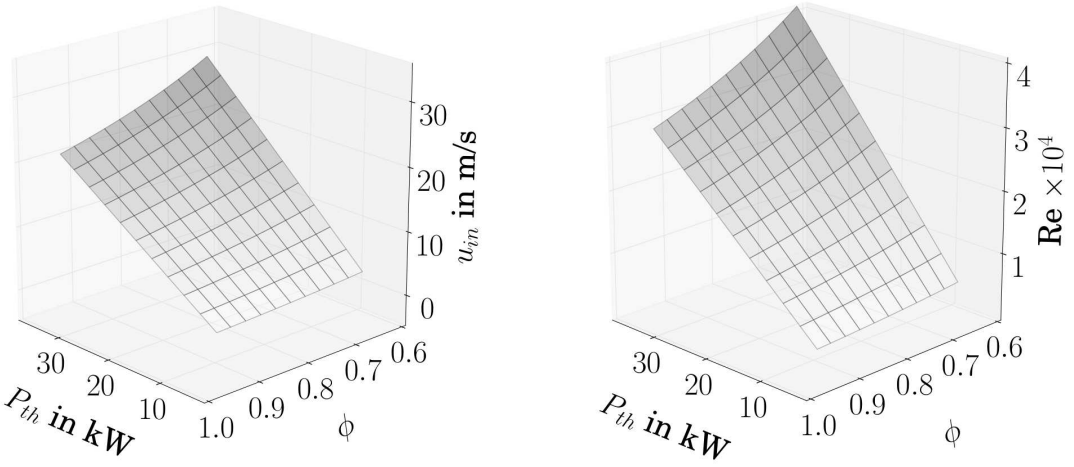


(a) Bulk velocity distribution.

(b) Reynolds number distribution.

**Fig. 6 Bulk velocity and Reynolds number as function of thermal load and global equivalence ratio for the PRECCINSTA burner test case.**

## VII. CFD Results

First, qualitative CFD results and opposition with experimental data of the case $P_{\text{th}} = 25\text{kW}, \Phi = 0.9$ are shown for mid-plane sections in the combustion chamber in Fig. 7. As can be seen in Figs. 7(a) and (b), the URANS simulation reproduces the experimentally measured flow field nicely. All characteristics of the recirculation zones as well as the expansion angle of the flow are accurately described. The comparison of mean temperature and temperature RMS in Figs. 7(c) and (d) shows that combustion is also well depicted with the employed numerical methods. The flame in the numerical simulation stabilizes in the inner recirculation zone, as indicated by Raman measurements. The opening angle of the flame matches with experimental data. The previously introduced transport equation for the evaluation of temperature variance in the simulation as post-processing step, Eq. (9), is evaluated with modeled turbulence and flow field quantities from the URANS simulation and gives a good representation of fluctuating temperature values.

Those findings are confirmed by the quantitative comparison of simulation and measurements on horizontal profile lines in the combustion chamber, as shown in Fig. 8. Flow field quantities are representatively shown with absolute velocity. For all positions in the combustion chamber, experimental flow field profiles are reproduced in the simulation with high accuracy. The same holds for temperature profiles in Fig. 8(b). The opening angle of the flame as well as absolute levels are nicely captured. The quantitative results of reproduction of temperature RMS profiles in Fig. 8(c) however reveal weaknesses of the chosen approach of using an additional transport equation for the determination of temperature variance field solutions based on given flow field and turbulence quantities, especially in the vicinity of the burner axis, where fluctuation is clearly overpredicted in the numerical simulation. Nonetheless, peak values of the profiles are captured well, which is crucial for a successful application of the combustion noise sound source reconstruction approach and a prediction of absolute combustion noise levels without further tuning of the approach.

Additionally, the combustion parameters thermal load and equivalence ratio, which are explicitly varied in this study for their impact on combustion noise emission, are correlated with integral heat release and the integral of $\varphi$ from Eq. (26), indicating contributions to combustion noise in the combustion chamber. Results are shown in Fig. 9. As expected, an increase in thermal load corresponds to a larger entry of global heat release in the combustion chamber. The correlation in Fig. 9(a) shows a linear relation between thermal load and integral heat release for both investigated equivalence ratios, $\phi = 0.8$ and $\phi = 0.9$. A linear correlation with however different slope is observed for the integral of $\varphi$ as a function of thermal load. $\varphi$ as an indicator for contributions to combustion noise in the combustor therefore seems to strongly correspond to the overall heat release entry. Furthermore it can be stated from the results in Fig. 9(a) and (b) that CFD simulations deliver plausible results in terms of heat release entries for different thermal loads.
The same is observed for the correlation of integral heat release and the integral $\varphi$ with global equivalence ratio, where both (Fig. 9(c) and Fig. 9(d)) show very similar trends. However, a variation of global equivalence ratio has only weak dependencies on integral heat release and $\varphi$, for the different investigated thermal loads.

Additionally, quantities influencing the effectively realized source term variance $\varphi$ are correlated with the integral entry of $\varphi$ in the combustion chamber. Results are depicted in Fig. 10. Investigated integral parameters are temperature $T$, RMS of temperature $T_{RMS}$, integral lengthscale $l_T$ and integral timescale $\tau_T$. Different operation points with varying thermal load are shown and multiple points for each thermal load denote the different equivalence ratios. As detected in the previously shown correlations, variations in equivalence ratio do not significantly contribute to a variation of overall combustion noise entries (Fig. 10 (a) and (b)). Different load points with varying equivalence ratio but constant thermal load are more or less horizontally aligned. Contrarily, a variation in thermal load significantly changes the values for integral source variance in the combustion chamber. However, no unique correlation between either temperature and source variance $\varphi$ or temperature RMS and source variance can be identified. A different picture holds for the integral turbulence scales shown in Fig. 10 (c) and (d). For increasing thermal loads and therefore combustor inlet velocities, larger lengthscales are present, leading to increased source variance levels. This corresponds to spatially larger sound sources in the combustion chamber for increased thermal loads. Higher inlet velocities furthermore induce stronger turbulent decay, as can be seen in Fig. 10(d), where smaller integral timescales are present for higher thermal loads. Integral quantities in the combustion chamber are analyzed due to the fact that the overall flow and combustion is in all cases swirl stabilized, with the flame being located in the inner recirculation zone.

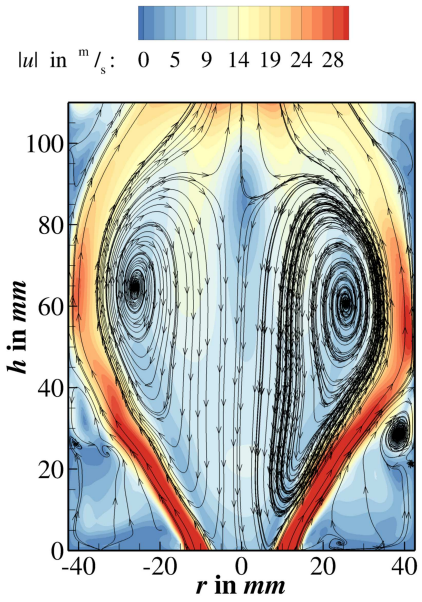


(a) Absolute velocity. Contours: CFD, streamlines: PIV.

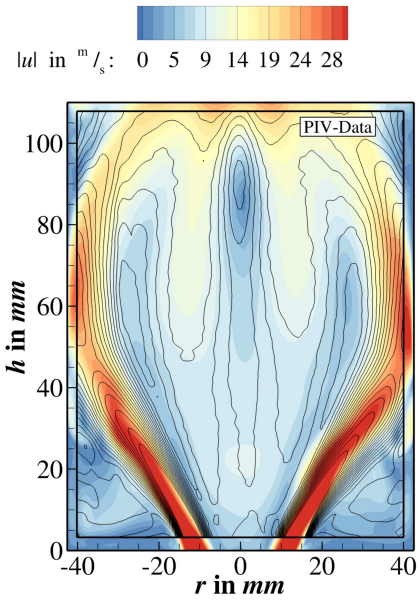


(b) Absolute velocity. Contours: CFD, level curves: PIV.

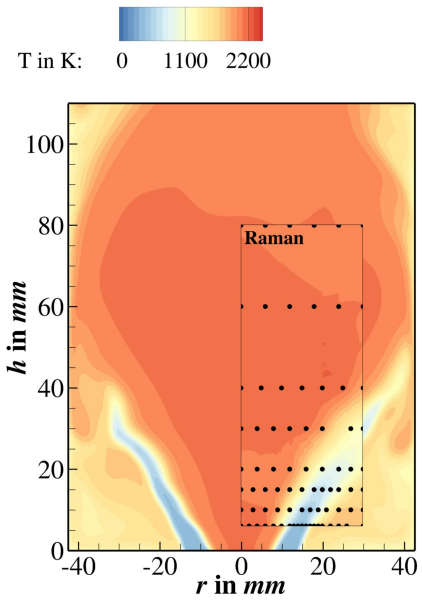


(c) Temperature. Contours: CFD, window: Raman measurements.

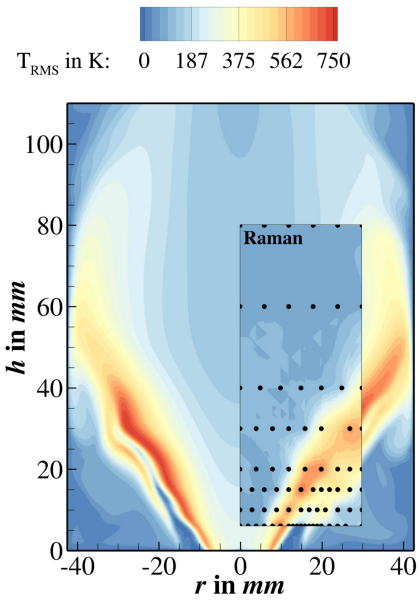


(d) RMS of Temperature. Contours: CFD, window: Raman measurements.

**Fig. 7 Qualitative comparison of CFD URANS simulation results with experimental data [17].** $P_{\text{th}} = 25\text{kW}, \Phi = 0.9$**.**

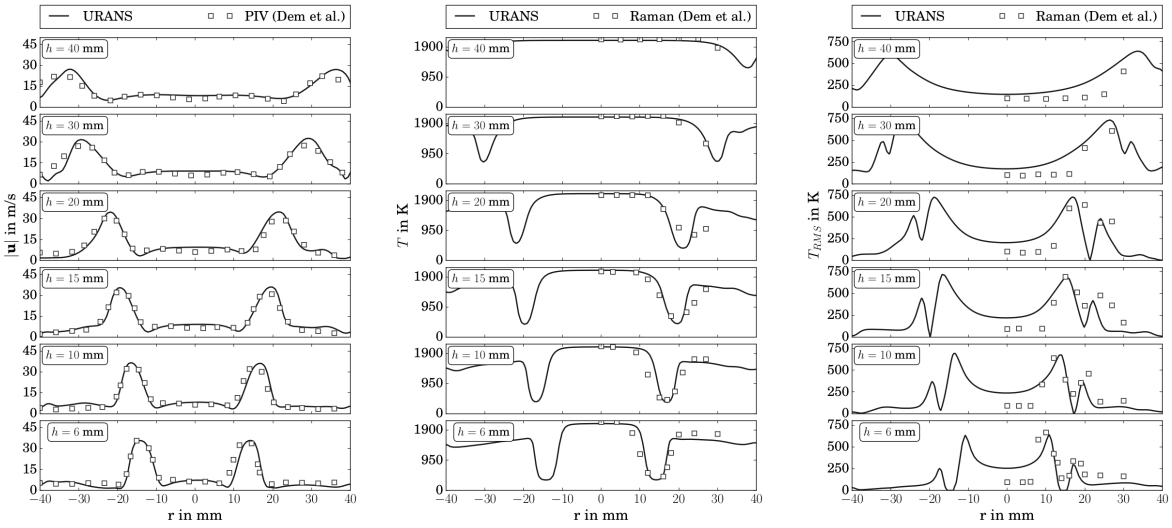


(a) Absolute velocity. (b) Temperature. (c) RMS of temperature.

**Fig. 8 Quantitative comparison of CFD URANS simulation results with experimental data [17].** $P_{\text{th}} = 25\text{kW}, \Phi = 0.9$**.**

## VIII. Computational Combustion Acoustics Setup

Computational combustion acoustics simulations are carried out with the DLR inhouse code PIANO (Perturbation Investigation of Aerodynamic Noise) [42]. PIANO is employed for the sound propagation modeling via linearized Euler equations. Sound sources are reconstructed from local turbulence statistics as an input from the preceding CFD RANS simulations. Stochastic sound source reconstruction is performed at each time step with the integrated module FRPM (Fast Random Particle Method).

The computational grid for the acoustics simulations is shown in Fig. 11. The finite-difference based dispersion relation preserving Scheme (DRP) from Tam & Webb [43] is employed for spatial discretization. The block-structured grid in Fig. 11 consists of 1.5M hexahedra with 1.94M nodes in 938 blocks. It spatially resolves frequencies up to $f_{max} = 15\text{kHz}$. For solution proceeding in time, a classical four-step Runge Kutta scheme is used. The mesh is optimized with respect to the local growth rate of adjacent cells with a maximum growth rate in critical regions of 1.05. Those are zones with large velocity and density gradients close to the combustor inlet and in the reaction zone. Mean flow field quantities $\overline{\rho}, \tilde{u}, \tilde{v}, \tilde{w}, \overline{p}$ are interpolated from the unstructured CFD RANS grid to the CCA domains using a statistical Kriging [44] algorithm for each investigated operation condition.

The overall simulation time step is limited by the sound propagation modeling and depends on the grid size as well as the local Mach number according to $\Delta t_{max} = (2.83\Delta x_{min})/(\pi + \pi Ma)$. Therefore, a time-step of $\Delta t = 2.2 \cdot 10^{-7}\text{s}$ is used. The cell determining the maximum time step is located in the combustor outlet tube, where a composition of hot combustion products is present.

The computational domain is enclosed by non-reflecting radiation boundary conditions [43] at the air plenum inlet tube, as shown in Fig. 11. An additional plenum is attached to the combustor outlet, which is in turn enclosed by a damping sponge layer and radiation conditions. Walls are modeled as fully reflecting, while the ghost point concept of Tam & Dong [45] is used. As the main criterion for the determination of source field extensions, field values larger than 5% of the peak value of $\varphi$ in the inner shear layer are included. This leads to source field extensions of $x \in [-10\text{mm}; 50\text{mm}]$ and $y, z \in [-38\text{mm}; 38\text{mm}]$. Sources are reconstructed on an auxiliary equidistant and orthogonal grid, with $\Delta = 1\text{mm}$, which results in 346.6K cells and an initial distribution of random particles with 1.154 particles per cell. Sources are obtained via recursive filtering [30, 31] operations along the auxiliary grid, accounting for the local integral length scale. Turbulence is synthesized with a first order Langevin approach, as introduced with Eqs. (11) to (13). Integral one-point statistics are extracted from the preceding CFD RANS simulations according to

$$l_T = \frac{\sqrt{k}}{\beta^* \omega} \quad \text{and} \quad \tau_T = \frac{1}{\beta^* \omega}. \tag{27}$$

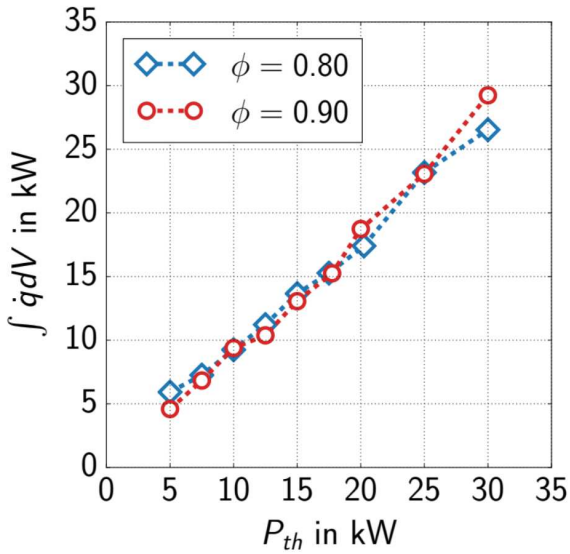


(a) Integrated heat release for varying thermal load.

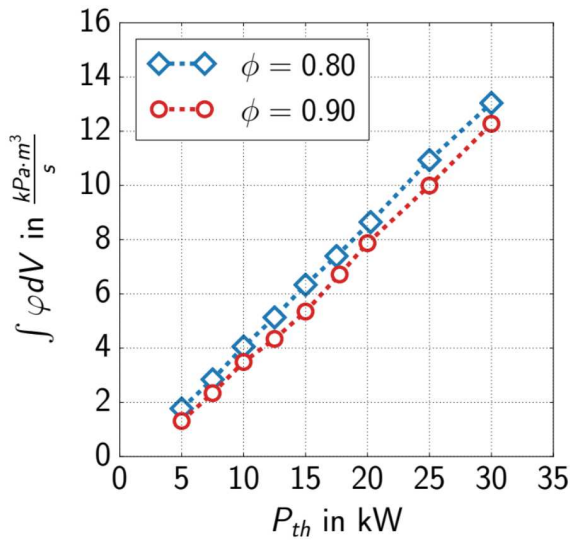


(b) Integrated averaged combustion noise source term profiles for varying thermal load.

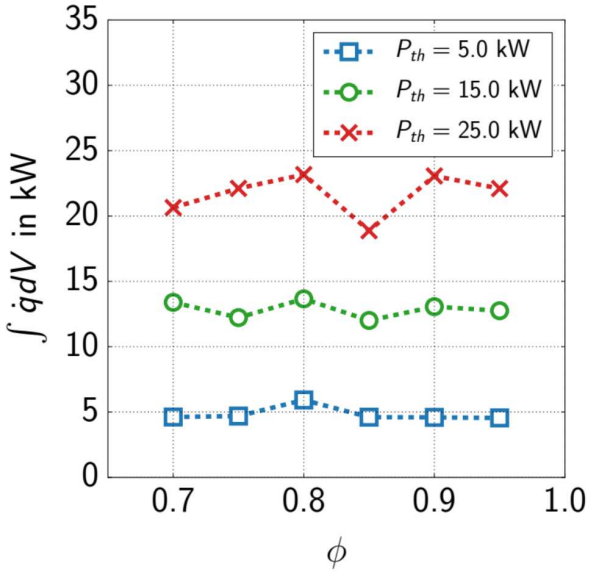


(c) Integrated heat release for varying global equivalence ratio.

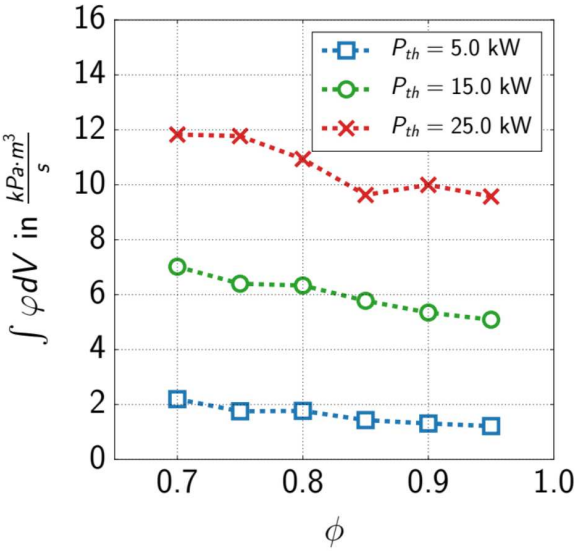


(d) Integrated averaged combustion noise source term profiles for varying global equivalence ratio.

**Fig. 9 Integrated CFD heat release rate and averaged combustion noise source term profiles as a function of thermal load and global equivalence ratio.**

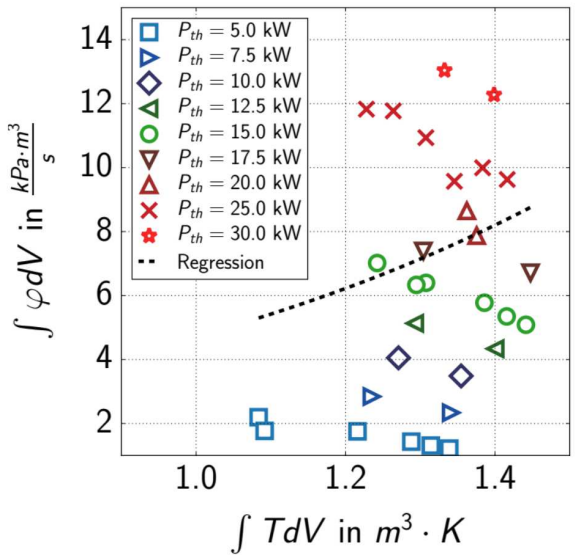


(a) Integral correlation of combustion temperatures and source term profiles $\varphi$.

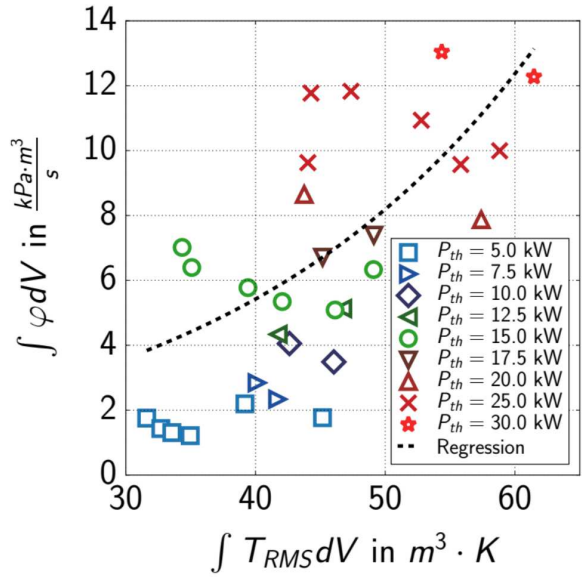


(b) Integral correlation of combustion rms temperatures and source term profiles $\varphi$.

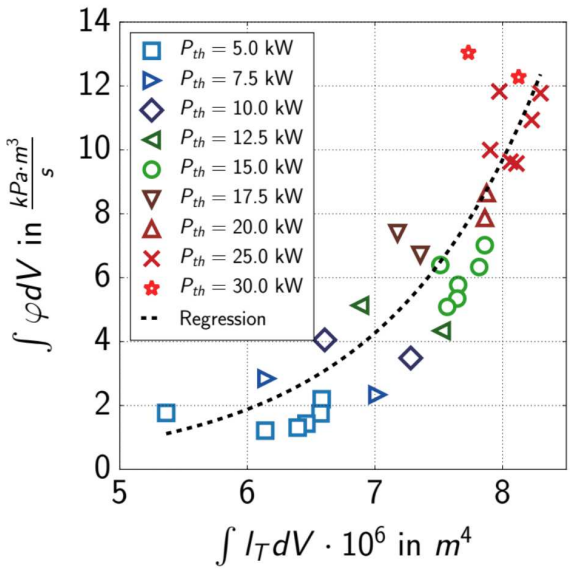


(c) Integral correlation of integral length-scales and source term profiles $\varphi$.

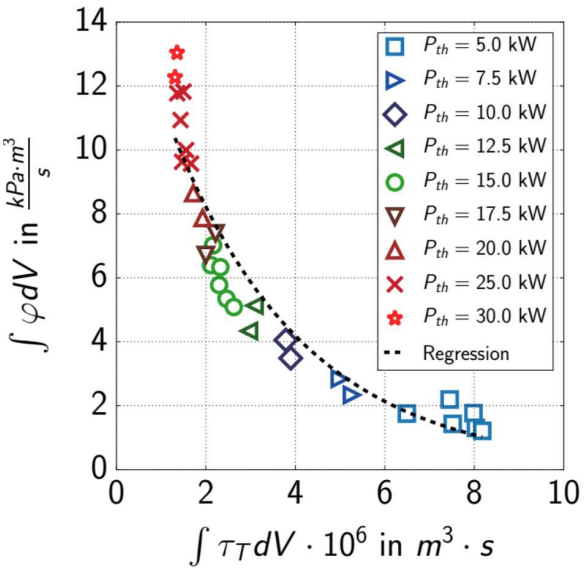


(d) Integral correlation of integral time-scales and source term profiles $\varphi$.

**Fig. 10 Inter-correlation analysis of flow turbulence and combustion parameters with impact on the combustion noise source term. Integral analysis in the combustion chamber for mean temperature, rms of temperature, integral length- and time-scales against integrated contributions to combustion noise sources according to $\varphi = (\gamma \overline{p})/\tilde{T}(\widetilde{T''^2}/\tau_T^2)^{0.5}$.**

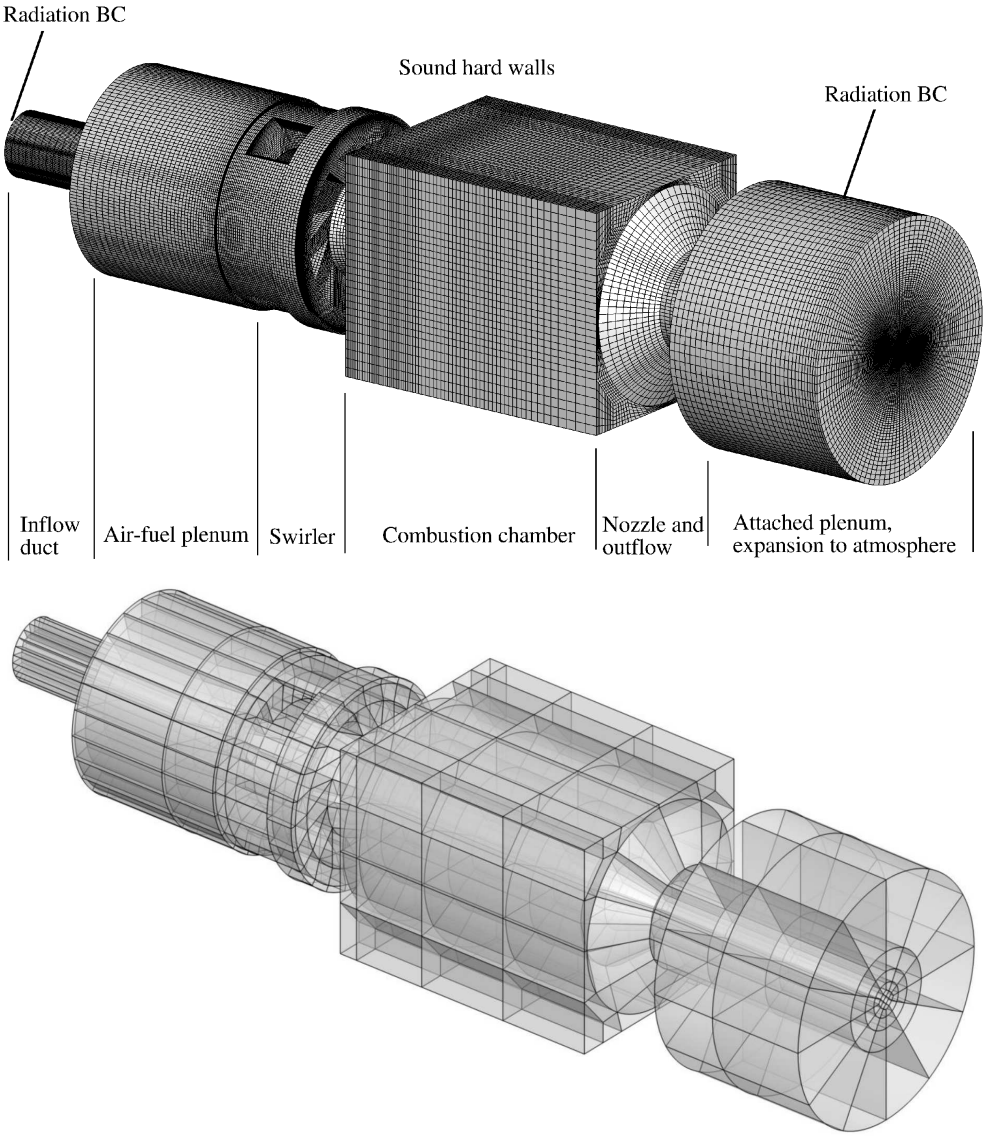


**Fig. 11 CCA computational grid with applied boundary conditions and labeled burner sections (top). Block structure of the computational domain (bottom).**

A total of $N_{CCA} = 9 \cdot 10^5$ time steps is simulated, while resulting sound pressure spectra are evaluated over a time span of $\Delta t_{overall} = 0.2$s.

## IX. Computational Combustion Acoustics Results

Stochastic combustion noise sound sources are reconstructed based on integral turbulence statistics in the combustion chamber, as shown in Fig. 12(b). An exemplary distribution of instantaneous combustion induced sound pressure and sound sources in the inner shear layer are shown in Fig. 12(a). Largest sound pressure levels occur close to the combustor front plate. The combustor exit is surrounded by an additional plenum and therefore acts as partially reflecting.

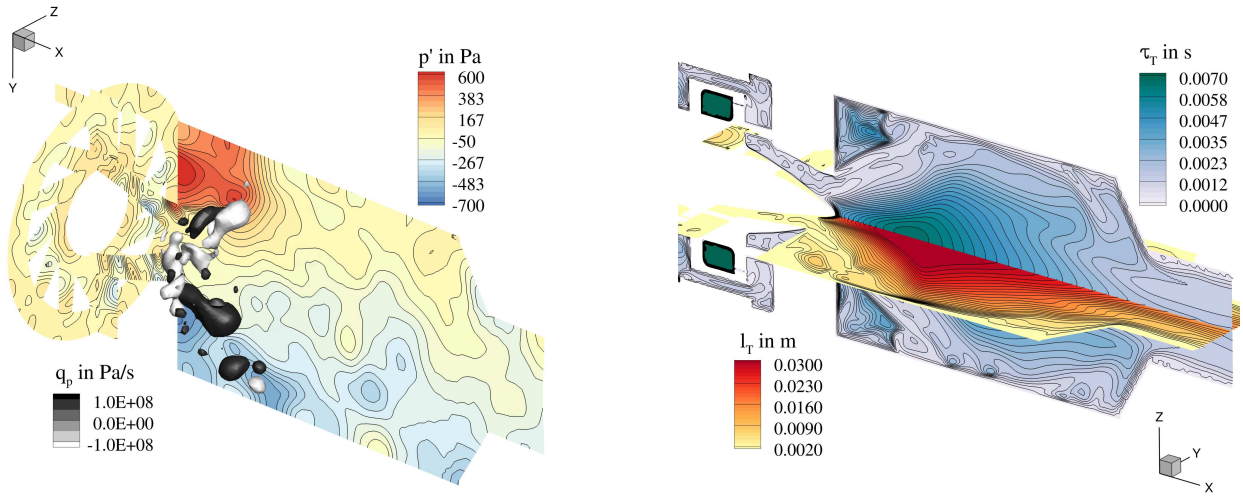


(a) Instantaneous distribution of combustion noise sound sources (iso-contours) and sound pressure in the combustion chamber.

(b) Field solution of integral turbulence scales in the combustor, time-scale (vertical layer) and length-scale (horizontal layer).

**Fig. 12 Exemplary results from combustion acoustics simulations.**

Peak acoustic pressure distribution in the combustion chamber can be explained by looking at frequency band filtered acoustic pressure, carried out by selective frequency filtering, as previously introduced. Results for acoustic pressure and different frequency bands are shown in Fig. 14. Conventions and locations of investigated planes in the combustor are shown in Fig. 13. The signal is decomposed in the frequency domain, and the harmonized signals for a certain frequency band are summarized. The averaged re-transformed acoustic pressure results are depicted. From Fig. 14 it becomes clear that the large acoustic pressure fluctuations in the upstream corners of the combustion chamber are high frequency resonance modes, which stabilize close to the combustor front plate. For example, in the frequency band of $f \in$[6000;6300]Hz a transverse rotating mode exists with one node in longitudinal direction and one node in the transverse plane, parallel to the combustion chamber front wall. Transverse oscillations are present for multiple frequency bands, as for example also for $f \in$[4700;5100]Hz. The overlay of the different high frequency transverse modes amounts to the locally large pressure fluctuations as can be seen in Fig. 12a. All numerical results show high frequency oscillations, which are however not captured in the experiments due to microphone calibration for up to 2000Hz only.

Furthermore, as indicated in Fig. 12b, acoustic sound sources fluctuating at large frequencies - corresponding to small integral time-scales - should predominantly occur at the flame root close to the combustion chamber inlet region. Larger turbulent time-scales downstream and closer to the combustion chamber side walls should then correspond to low-frequency fluctuating acoustic sound sources.

This is verified with frequency filtered fluctuating acoustic sound sources, which are shown for different frequency bands in Fig. 15. For lower frequency bands, stronger contributions by sound sources to the overall combustion induced acoustic energy are observed rather downstream (Fig. 15a), while the opposite can be seen for higher frequency bands in Fig. 15c. Therefore, 3D FRPM-CN exhibits a correct conversion of integral turbulence statistics to sound source dynamics in this complex, swirl stabilized application case.

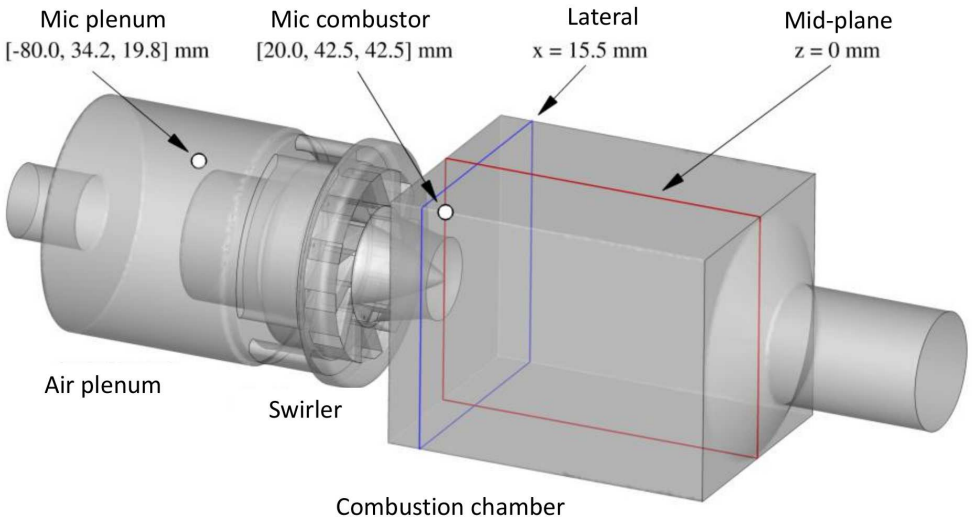


**Fig. 13 Conventions for computational combustion acoustics analyses.**

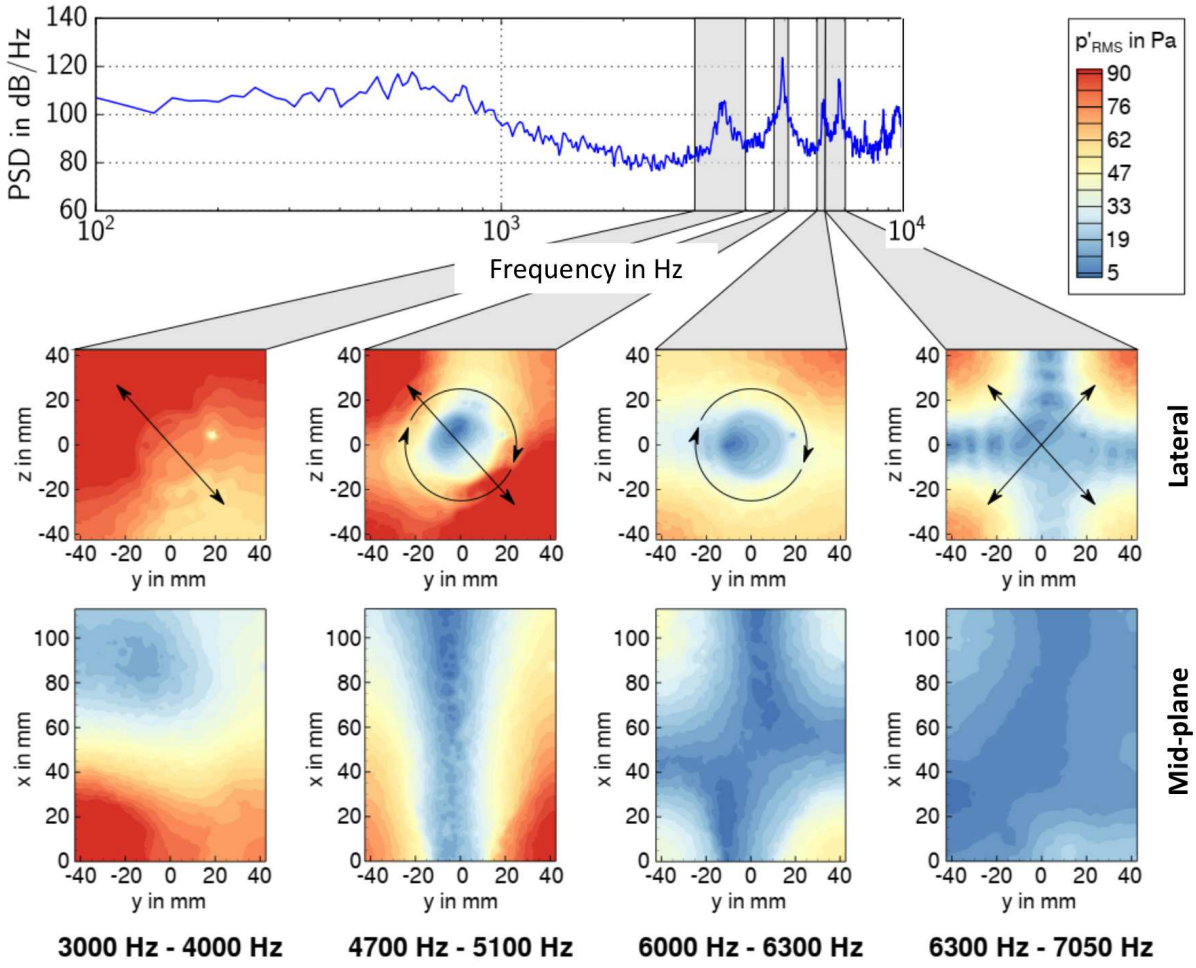


**Fig. 14 Frequency-band filtered (SFFFA) root mean square of high frequency acoustic pressure modes in the combustion chamber. Arrows denote direction of oscillation.**

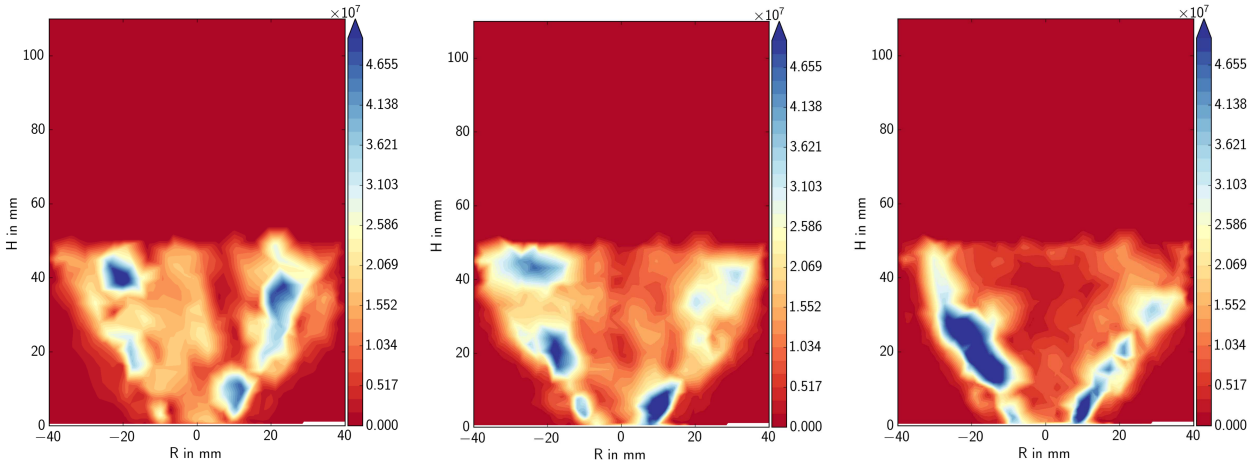


(a) $f$ ∈[50;200]Hz. (b) $f$ ∈[200;500]Hz. (c) $f$ ∈[1000;2000]Hz.

**Fig. 15 Frequency-band filtered (SFFFA) fluctuating acoustic noise sources in a vertical combustor mid-plane in [Pa/s].**

A comparison of experimental sound pressure spectra and numerical simulations for varying thermal load and a constant global equivalence ratio $\phi = 0.9$ are depicted in Fig. 16. Experimental data is calibrated for up to $f = 2$kHz only. Spectra are shown for a combustion chamber and an air plenum microphone according to Fig. 3. As expected, sound pressure levels globally decrease for smaller thermal load entries and vice versa. Two peaks are present in the experimental data, which can be assigned to a longitudinally oscillating thermoacoustic instability and its first harmonic [46], which cannot be captured by the sequential FRPM-CN approach.
Remarkably, the pressure spectra in combustion chamber and upstream air plenum have a similar, characteristic shape for all treated operation conditions. Levels are lower for smaller frequencies and then increase up to a certain level, whereas there is a characteristic roll-off for higher frequencies. The numerical simulations tend to reproduce those characteristic shapes well, despite low frequency fractions for $P_{th} = 20,25$kW and $P_{th} = 12.5$kW in the combustion chamber. Numerical simulations are carried out without artificial scaling, solely relying on input of temperature variance, mean flow field and integral turbulence statistics from preceding reacting CFD simulations. Therefore, absolute noise sound pressure levels are accurately captured for most of the operation conditions, not only in the combustion chamber, but also in the upstream fuel-air plenum. Results are least satisfactory in terms of agreement with experimental data for operation points with small thermal loads, especially at $P_{th} = 5$kW. This could be linked to difficulties in stabilizing the flame in the preceding URANS simulations and therefrom resulting insufficient flow field, combustion, and turbulence statistics.

A different picture is found for a comparison of experiment and CFD simulation of sound pressure spectra for varying global equivalence ratio and constant thermal load $P_{th} = 25$kW, shown in Fig. 17. Still, absolute sound pressure levels are nicely captured for some points, whereas there are larger deviations for low or high frequencies at several operation conditions. Therefore, it seems that prediction of sensitive changes in combustion parameters as in a variation of global equivalence ratio is difficult with a hybrid method relying on robust but accuracy-deficient RANS models in the first place. However, experiments indicate that there is a significant change in spectral shape from a variation of global equivalence ratio.

Therefore, it can be summarized that 3D FRPM-CN is well suited for the prediction of absolute combustion noise levels, even in enclosed configurations with complex flow field and combustion. Even the general characteristic shape of the sound pressure spectra is well described with the method. However, if one is interested in very accurate predictions of local sound pressure over a large range of frequencies with very limited deviations, scale resolving, compressible CFD simulations are necessary, which are up to now still computationally expensive and difficult to handle.
Another advantage of hybrid approaches compared to direct numerical assessment of technical relevant cases comes into play. Hybrid approaches are usually decoupled and therefore rather simple models for the depiction of noise

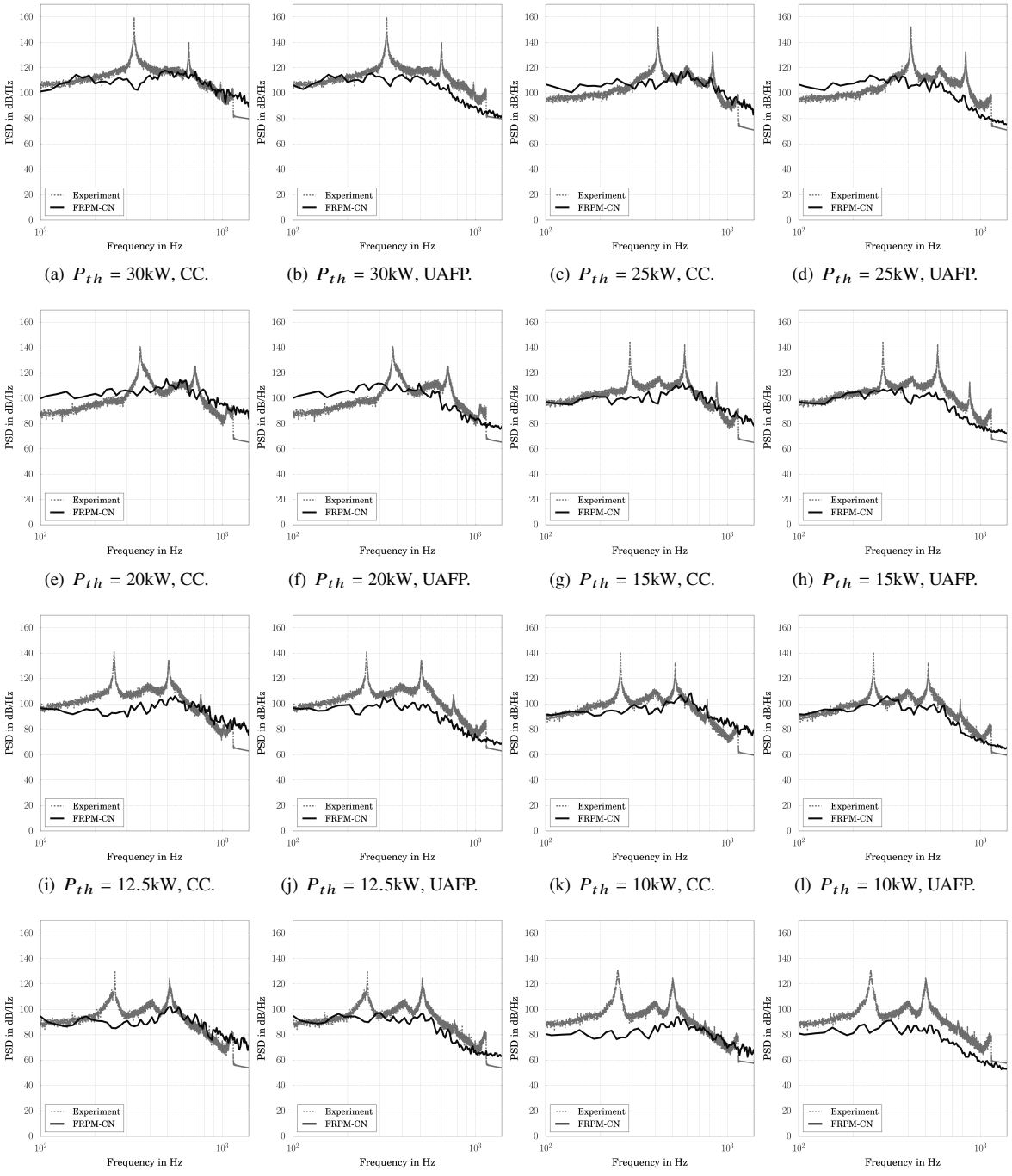


(a) $P_{th}$ = 30kW, CC. (b) $P_{th}$ = 30kW, UAFP. (c) $P_{th}$ = 25kW, CC. (d) $P_{th}$ = 25kW, UAFP.

(e) $P_{th}$ = 20kW, CC. (f) $P_{th}$ = 20kW, UAFP. (g) $P_{th}$ = 15kW, CC. (h) $P_{th}$ = 15kW, UAFP.

(i) $P_{th}$ = 12.5kW, CC. (j) $P_{th}$ = 12.5kW, UAFP. (k) $P_{th}$ = 10kW, CC. (l) $P_{th}$ = 10kW, UAFP.

(m) $P_{th}$ = 7.5kW, CC. (n) $P_{th}$ = 7.5kW, UAFP. (o) $P_{th}$ = 5kW, CC. (p) $P_{th}$ = 5kW, UAFP.

**Fig. 16 Comparison of 3D FRPM-CN results with experimental pressure spectra. Variation of thermal load $P_{th}$ for constant global equivalence ratio $\Phi = 0.9$. CC: Combustion chamber microphone, UAFP: Upstream air-fuel plenum.**

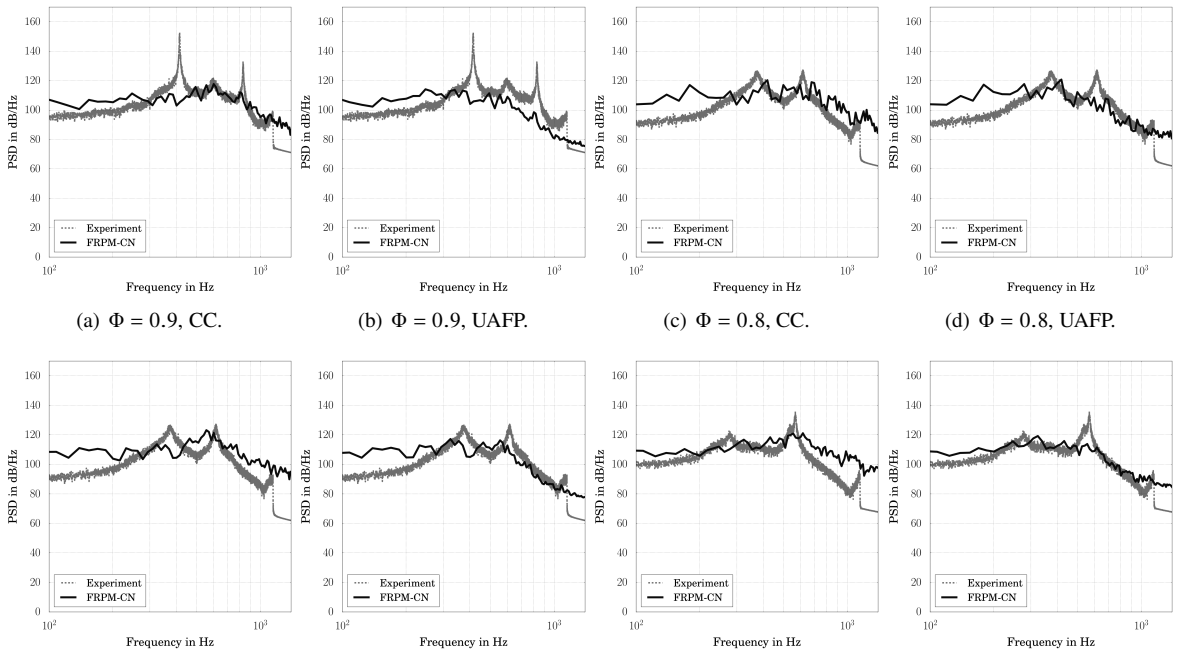


(a) $\Phi = 0.9$, CC. (b) $\Phi = 0.9$, UAFP. (c) $\Phi = 0.8$, CC. (d) $\Phi = 0.8$, UAFP.

(e) $\Phi = 0.75$, CC. (f) $\Phi = 0.75$, UAFP. (g) $\Phi = 0.7$, CC. (h) $\Phi = 0.7$, UAFP.

**Fig. 17 Comparison of 3D FRPM-CN results with experimental pressure spectra. Variation of global equivalence ratio $\Phi$ for constant thermal load $P_{th} = 25$kW. CC: Combustion chamber microphone, UAFP: Upstream air-fuel plenum.**

damping effects can be implemented. In that case, design processes of acoustic liner systems in combustion chambers can be carried out in an efficient but yet simplified way.

## X. Conclusions

The CFD URANS simulations of the PRECCINSTA burner were conducted on two Intel Ivy Bridge E5 nodes, with 12 cores each with 2.4GHz and memory of 64Gb. For the simulation of one operation point, including cold flow simulation and several iteration steps for combustion, 1011CPU-h were necessary. A partially scale resolving LES/URANS simulation with moderate spatial and temporal resolution (around 80-90% of the turbulent kinetic energy directly resolved) of the same case, which was not explicitly shown in the paper, costed around 38000CPU-h. Considering the quality of agreement of CFD RANS results shown in the paper with experimental data, the RANS methods exhibit a highly satisfactory performance at very low computational costs, if one is interested in averaged flow field and combustion quantities. However, as was demonstrated further on, additional transport equations for higher order moments, as for the temperature variance, also show high quality results in comparison with experimental data. Combustion acoustics simulations with the hybrid 3D FRPM-CN approach were carried out on the same node architecture in 2700CPU-h. Therefore, the process chain of CFD plus additional CCA simulation amount to around 3700CPU-h, while approximately additional 15CPU-h were necessary for the interpolation of CFD flow and temperature field onto the combustion acoustics domain. In case a scale-resolving, fully compressible CFD simulation would be carried out in order to obtain combustion acoustics numerically, those turnaround times would be exceeded by far. Therefore, the numerical approach used in this work is a highly efficient and accurate approach for the determination of combustion noise, even in encased configurations with highly complex and highly turbulent flows.

On the experimental side, a novel data set of acoustics measurements for the PRECCINSTA laboratory burner with rigid metal combustion chamber walls was introduced, which served as validation basis for the combustion acoustics simulations. Variations of thermal load and global equivalence ratio and their impact on combustion acoustics noise levels were investigated. The experimental and the numerical results consistently showed a decrease of noise levels for lower thermal loads whereas noise levels stayed fairly constant with frequency dependent variation for an alteration of global equivalence ratios. It was found that the numerical approach FRPM-CN was able to accurately capture spectral

shapes and absolute sound pressure levels of experiments without any artificial scaling but showed inaccuracies in predicting the trends of global equivalence ratio variations in terms of acoustics. Experimental data furthermore revealed the presence of thermoacoustic oscillations in all investigated cases. Therefore, the measured data can be used as a validation basis of numerical approaches for the prediction of thermoacoustic instabilities, which was however not subject of the present study.
As commonly known, sequential and hybrid approaches cannot capture thermoacoustics without two-way coupling of CFD and acoustics and resolution of transient phenomena. However, by using an approach for selective Fourier filtering in frequency domain, it was shown that characteristic acoustic modes can be detected numerically.

## References


[1] ACARE, "Strategic Research Agenda, Volume 1," 2001. Www.acare4europe.org.

[2] European Comission, "European Aeronautics: A Vision for 2020," 2001. Office for Official Publications of the European Communities, Luxembourg, Luxembourg, ISBN 92-894-0559-7.

[3] European Comission, "Flightpath 2050: Europe's Vision for Aviation," 2011. Office for Official Publications of the European Communities, Luxembourg, Luxembourg, ISBN 978-92-79-19724-6, doi 10.2777/5026.

[4] Rolls-Royce, *The Jet Engine*, Technical Publications Department, Rolls-Royce plc, Derby, England, 1996. ISBN 10: 0902121235.

[5] Dowling, A., and Mahmoudi, Y., "Combustion noise," *Proceedings of the Combustion Institute*, Vol. 35, 2015, pp. 65–100.

[6] Tam, C., "On the Spectrum of Combustion Noise," *21st AIAA/CEAS Aeroacoustic Conference*, 2015.

[7] Bui, T., Schröder, W., and Meinke, M., "Numerical analysis of the acoustic field of reacting flows via acoustic perturbation equations," *Computers & Fluids*, Vol. 37, No. 9, 2008, pp. 1157–1169.

[8] Mühlbauer, B., Ewert, R., Kornow, O., Noll, B., Delfs, J., and Aigner, M., "Simulation of combustion noise using CAA with stochastic sound sources from RANS," *14th AIAA/CEAS Aeroacoustic Conference*, 2008. AIAA 2008-2944.

[9] Ewert, R., and Emunds, R., "CAA Slat Noise Studies Applying Stochastic Sound Sources Based On Solenoidal Digital Filters," *11th AIAA/CEAS Aeroacoustics Conference*, 2005.

[10] Ewert, R., "Slat Noise Trend Predictions Using CAA With Stochastic Sound Sources From A Random Particle-Mesh Method (RPM)," *12th AIAA/CEAS Aeroacoustics Conference*, 2006.

[11] Ewert, R., "RPM - the fast Random Particle-Mesh method to realize unsteady turbulent sound sources and velocity fields for CAA applications," *13th AIAA/CEAS Aeroacoustics Conference*, 2007.

[12] Ewert, R., "Broadband Slat Noise Prediction Based on CAA and Stochasic Sound Sources from a Fast Random Particle-Mesh (RPM) Method," *Computers and Fluids Journal*, Vol. 37, No. 4, 2008, pp. 369–387.

[13] Grimm, F., Ewert, R., Dierke, J., Noll, B., and Aigner, M., "Efficient Full 3D Turbulent Combustion Noise Simulation Based on Stochastic Sound Sources," *21st AIAA/CEAS Aeroacoustics Conference*, 2015. AIAA Paper 2015-2973.

[14] Grimm, F., Reichling, G., Ewert, R., Dierke, J., Noll, B., and Aigner, M., "Efficient Combustion Noise Simulation of a Gas Turbine Model Combustor Based on Stochastic Sound Sources," *Proceedings of ASME Turbo Expo 2015*, 2015. GT2015-42390.

[15] Mühlbauer, B., Ewert, R., Kornow, O., and Noll, B., "Evaluation of the RPM Approach for the Simulation of Broadband Combustion Noise," *AIAA Journal*, Vol. 48, No. 7, 2010, pp. 1379–1390.

[16] Candel, S., Durox, D., Ducruix, S., Birbaud, A.-L., Noiray, N., and Schuller, T., "Flame dynamics and combustion noise: progress and challenges," *International Journal of Aeroacoustics*, Vol. 8, No. 1, 2009, pp. 1–56.

[17] Dem, C., Stöhr, M., Arndt, C., Steinberg, A., and Meier, W., "Experimental study of turbulence-chemistry interactions in confined swirl flames with different degrees of premixing," *Zeitschrift für Physikalische Chemie*, Vol. 229, No. 4, 2015, pp. 569–585.

[18] Oberleithner, K., Stöhr, M., Im, S., Arndt, C., and Steinberg, A., "Formation and flame-induced suppression of the precessing vortex core in a swirl combustor: Experiments and linear stability analysis," *Combustion and Flame*, Vol. 162, No. 8, 2015, pp. 3100–3114.

[19] Meier, W., Weigand, P., Duan, X., and Giezendanner-Thoben, R., "Detailed characterization of the dynamics of thermoacoustic pulsations in a lean premixed swirl flame," *Combustion and Flame*, Vol. 150, 2007, pp. 2–26.

[20] Domenico, M. D., "Numerical simulations of soot formation in turbulent flows," Dissertation, Institut für Verbrennungstechnik der Luft- und Raumfahrt, Universität Stuttgart, 2008. Http://elib.uni-stuttgart.de/opus/volltexte/2008/3624/.

[21] Reichling, G., Noll, B., and Aigner, M., "Development of a Projection-Based Method for the Numerical Calculation of Compressible Reactive Flows," *Proceedings of the 51st AIAA Aerospace Sciences Meeting including the New Horizons Forum and Aerospace Exposition*, 2013. AIAA 2013-1003.

[22] Reichling, G., Noll, B., and Aigner, M., "Numerical Simulation of the Non-Reactive and Reactive Flow in a Swirled Model Gas Turbine Combustor," *21st AIAA Computational Fluid Dynamics Conference*, 2013. AIAA 2013-2434.

[23] Reichling, G., "Development of Numerical Methods for the Calculation of Thermo-Acoustic Interactions in Gas Turbine Combustion Chambers," Dissertation, Institut für Verbrennungstechnik der Luft- und Raumfahrt, Universität Stuttgart, 2015. Http://elib.uni-stuttgart.de/opus/volltexte/2015/9922/.

[24] Grimm, F., Ohno, D., Werner, S., Stöhr, M., Ewert, R., Dierke, J., Noll, B., and Aigner, M., "Direct Combustion Noise Simulation of a Lean Premixed Swirl Flame using Stochastic Sound Sources," *54th AIAA Aerospace Sciences Meeting, AIAA Science and Technology Forum and Exposition 2016*, 2016. AIAA Paper 2016-1881.

[25] Lourier, J., Stoehr, M., Noll, B., Werner, S., and Fiolitakis, A., "Scale Adaptive Simulation of a thermoacoustic instability in a partially premixed lean swirl combustor," *Combustion and Flame*, Vol. 183, 2017, pp. 343–357.

[26] Mühlbauer, B., Ewert, R., Kornow, O., Boyde, J., Noll, B., Delfs, J., and Aigner, M., "Evaluation of the RPM-CN approach for broadband combustion noise prediction," *15th AIAA/CEAS Aeroacoustic Conference*, 2009. AIAA 2009-3285.

[27] Grimm, F., Ewert, R., Dierke, J., Noll, B., and Aigner, M., "The Fast Random Particle Method for Combustion Noise Prediction," *20th AIAA/CEAS Aeroacoustics Conference*, 2014. AIAA Paper 2014-2451.

[28] Ewert, R., Kornow, O., Delfs, J., Yin, J., Röber, T., and Rose, M., "A CAA Based Approach to Tone Haystacking," *15th AIAA/CEAS Aeroacoustics Conference*, 2009.

[29] Grimm, F., Ewert, R., Dierke, J., Noll, B., and Aigner, M., "Broadband Combustion Noise Prediction with the Fast Random Particle Method," *Proceedings of ASME Turbo Expo 2014*, 2014. GT2014-25195.

[30] Purser, R., Wu, W.-S., Parrish, D., and Roberts, N., "Numerical aspects of the application of recursive filters to variational statistical analysis. part i: Spatially homogeneous and isotropic gaussian covariances," *Monthly Weather Review*, Vol. 131, 2003, pp. 1524–1535.

[31] Purser, R., Wu, W.-S., Parrish, D., and Roberts, N., "Numerical aspects of the application of recursive filters to variational statistical analysis. part ii: Spatially inhomogeneous and anisotropic gaussian covariances," *Monthly Weather Review*, Vol. 131, 2003, pp. 1536–1548.

[32] Grimm, F., Lourier, J., Lammel, O., Noll, B., and Aigner, M., "A Selective Fast Fourier Filtering Approach Applied to High Frequency Thermoacoustic Instability Analysis," *Proceedings of ASME Turbo Expo 2017*, 2017. GT2017-63234.

[33] Heinzel, G., Rüdiger, A., and Schilling, R., "Spectrum and Spectral Density Estimation by the Discrete Fourier transform (DFT), including a Comprehensive List of Window Functions and some new Flat-Top Windows," 2002.

[34] Cooley, J. W., and Tukey, J. W., "An algorithm for the machine calculation of complex Fourier series," *Mathematics of computation*, Vol. 19, No. 90, 1965, pp. 297–301.

[35] Alessio, S. M., *Digital Signal Processing and Spectral Analysis for Scientists*, Springer-Verlag, 2016. ISBN 978-3-319-25468-5.

[36] Domenico, M. D., "Private Kommunikation," 2015.

[37] Grimm, F., Noll, B., Aigner, M., Dierke, J., and Ewert, R., "Modeling of Combustion Acoustics Sources and their Dynamics in the PRECCINSTA Burner Testcase," *Thermoacoustic Instabilities in Gas Turbines and Rocket Engines: Industry meets Academia*, 2016. GTRE-003.

[38] Domenico, M. D., Gerlinger, P., and Noll, B., "Numerical Simulations of Confined, Turbulent, Lean, Premixed Flames using a Detailed Chemistry Combustion Model," *Proceedings of the ASME Turbo Expo 2011*, 2011. GT2011-45520.

[39] Menter, F., Kuntz, M., and Langtry, R., "Ten Years of Industrial Experience with the SST Turbulence Model," *Turbulence, Heat and Mass Transfer 4, ed: K. Hanjalic, Y. Nagano, and M. Tummers, Begell House, Inc., Danbury, USA*, 2003, pp. 625–632.

[40] Nicol, D., Malte, P., Hamer, A., Roby, R., and Steele, R., "Development of a Five-Step Global Methane Oxidation-NO Formation Mechanism for Lean-Premixed Gas Turbine Combustion," *Journal of Engineering for Gas Turbines and Power*, Vol. 121, No. 2, 1999, pp. 272–280.

[41] Turns, S., *An Introduction to Combustion: Concepts and Applications*, WCB/McGraw-Hill, ISBN10: 0073380199, 2012.

[42] Delfs, J., Bauer, M., Ewert, R., Grogger, H., Lummer, M., and Lauke, T., *Numerical Simulation of Aerodynamic Noise with DLR's aeroacoustic code PIANO*, DLR - German Aerospace Center, Braunschweig, Germany, $5^{\text{th}}$ ed., 2008.

[43] Tam, C., and Webb, J., "Dispersion-Relation-Preserving Finite Difference Schemes for Computational Acoustics," *Journal of Computational Physics*, Vol. 107, No. 2, 1993, pp. 262–281.

[44] Krige, D., "A statistical approach to some basic mine valuation problems on the Witwatersrand," *J. of the Chem., Metal and Mining Soc. of South Africa*, Vol. 52, No. 6, 1951, pp. 119–139.

[45] Tam, C., and Dong, Z., "Wall boundary conditions for high-order finite-difference schemes in computational aeroacoustics," *Theoret. Comput. Fluid Dynamics*, Vol. 6, 1994, pp. 303–322.

[46] Lourier, J.-M., Noll, B., and Aigner, M., "Large Eddy Simulation of a Thermoacoustic Instability within a Swirl-Stabilized Burner using Impedance Boundary Conditions," *Proceedings of ASME Turbo Expo 2014*, 2014. GT2014-26200.